Modeling DC, RF and Noise behavior of GaN HEMTs using ASM-HEMT Compact Model

A. Dasgupta, S. Ghosh,
S. A. Ahsan and Y. S. Chauhan
Dept. of Electrical Engineering,
Indian Institute of Technology Kanpur, India.
Email: avirup@iitk.ac.in

S. Khandelwal
Dept. of Electrical Engineering
and Computer Science,
University of California Berkeley,
USA.

N. Defrance
Institute of Electronics,
Microelectronics and Nanotechnologies,
University of Lille, France.

***Abstract*—In this paper, we aim to present a surface potential based model for GaN High Electron Mobility Transistors. The model is computationally efficient by virtue of being analytical and can be accurately used for DC and RF predictions. It includes velocity saturation, access region resistance effects, temperature dependance and models for gate current and noise.**

***Index Terms*—GaN, HEMT, compact model, noise, gate current**

I. Introduction

GaN High electron mobility transistors (HEMTs) are promising candidates for high power and high frequency applications. Effective circuit design using these devices require fast and accurate models able to describe the behavior of the device under different working conditions. Previous work includes the empirical model proposed by Angelov et.al. [1] and the subsequent improved version by Sadi et.al. [2]. Table based models also exist [3], though they are in limited use. Empirical models usually fail to capture the underlying device physics, whereas table based models are based on given measurement sets and are generally not scalable.The need of the hour is a fast and efficient physical model. The existing physics based models [4–6] have intricate mathematical formulations and are computationally demanding.

Our model, ASM-HEMT (*Advanced Spice Model for High Electron Mobility Transistors*) , is a surface potential based model, which is often considered as the most physical one. The model is completely analytical and shows good accuracy for DC and RF simulations.

II. Model description

The following subsections describe the various key aspects of the ASM-HEMT model.

A. Surface potential and charges

The ASM-HEMT model is based on the surface potential formulation proposed by Khandelwal et. al. [7, 8]. The Fermi level is given as

$$E_{f,unified} = V_{go} - \frac{2V_t ln\left(1+e^{\frac{V_{go}}{2V_t}}\right)}{\frac{1}{H(V_{go,p})}+(C_g/qD)e^{-\frac{V_{go}}{2V_t}}} \quad (1)$$

where, $V_{go} = V_{gs} - V_{OFF}$, V_{OFF} being the cut-off voltage; V_t is the thermal voltage, C_g is the gate capacitance per unit area, q is the electronic charge and D is the density of states. $V_{go,p}$ is equal to V_{go} for gate voltages above the threshold voltage and is of the order of thermal voltage in the sub-threshold region. H captures the bias dependance of the fermi level for $V_{go} > V_{OFF}$ [7]. The formulation given in (1) is valid for all regions of operation and the surface potential is calculated as $\psi = E_f + V_x$, where V_x is the channel potential.

This surface potential formulation is used to calculate the charges. Writing the charge densiy n as $C_g(V_{go} - \psi)$, the gate charge is given as

$$Q_g = -\int_0^L qWndx = -\int_0^L qWC_g(V_{go}-\psi)dx \quad (2)$$

which yields (2) after integration. The source and drain charges are obtained using the Ward-Dutton partitioning scheme [10].

B. Drain current

Using the surface potential formulation as described, we can write the current equation as [9]

$$I_{ds} = \frac{\mu_{eff}C_g}{\sqrt{1+\theta_{sat}^2\psi_{ds}^2}}\frac{W}{L}\left(V_{go}-\psi_m+V_{th}\right)\left(\psi_{ds}\right)\left(1+\lambda V_{ds,eff}\right) \quad (3)$$

The velocity saturation effect is included in (3) through the velocity saturation parameter θ_{sat} and the channel length modulation effect through λ. Also, $\psi_{ds} = \psi_d - \psi_s$ and $\psi_m = (\psi_d + \psi_s)/2$. The mobility degradation due to the vertical field is also included in μ_{eff} as

$$\mu_{eff} = \frac{U0}{1+UA(V_{go}-\psi_m)+UB(V_{go}-\psi_m)^2} \quad (4)$$

The drain current implementation also includes effects of drain induced barrier lowering, included in the bias dependance of the cut-off voltage. The total source/drain access region resistance is implemented as a sum of the source/drain contact resistance and the bias dependent access region resistance.

C. Gate Current

The gate current can be divided into three components based on the mechanism. The current density for the Poole-Frenkel

$$Q_g = \frac{C_g LW}{V_{go} - \psi_m + V_t}\left[V_{go}^2 + \frac{\psi_d^2 + \psi_s^2 + \psi_d\psi_s}{3} - V_{go}(\psi_d + \psi_s - V_t) - V_t\psi_m\right] \quad (5)$$

$$I_{PF} = J_0\left[(\beta^3 E^{1.5} - 3\beta^2 E + 6\beta\sqrt{E} - 6) - \frac{B}{A\beta^2}(\beta^5 E^{2.5} - 5\beta^4 E^2 + 20\beta^3 E^{1.5} - 60\beta^2 E + 120\beta\sqrt{E} - 120)\right]_{E_S}^{E_D} \quad (6)$$

$$I_{TE} = W\int_0^L J_{TE0}\left[exp\left(\frac{V_g - \psi}{\eta V_t}\right) - 1\right]dx = J_1\left[exp\left(\frac{V_g - \psi}{\eta V_t}\right)\eta V_t((\eta - 1)V_t - V_g + \psi) - \psi(V_t + V_g) + 0.5\psi^2\right]_{\psi_s}^{\psi_d} \quad (7)$$

$$I_{TA} = W\int_0^L J_{TA0}\left[exp\left(\frac{V_g - \psi - V_0}{\eta V_t}\right) - 1\right]dx = J_2\left[exp\left(\frac{V_g - \psi - V_t}{\eta V_t}\right)\eta V_t(\psi - V_g) + \psi\,(0.5\psi - V_t - V_g)\right]_{\psi_s}^{\psi_d} \quad (8)$$

$$S_{if} = P_1(f)\frac{I_{ds}^2 LK}{C_g^2}\left[\Gamma_1 V_t C_g\left(\frac{1}{n_d} - \frac{1}{n_s}\right) + (\Gamma_1 + \Gamma_2 V_t C_g)ln\left(\frac{n_d}{n_s}\right) + (\Gamma_2 + \Gamma_3 V_t C_g)(n_s - n_d) + 0.5\Gamma_3(n_d^2 - n_s^2)\right] \quad (9)$$

$$S_{it} = \frac{4kT}{I_{ds}L_{eff}^2}\left[\left(\frac{\mu_{eff}}{\sqrt{1 + \theta_{sat}^2\psi_{ds}^2}}\right)WqC_g\right]^2\left(V_{go}^2\psi_{ds} + \frac{\psi_d^3 - \psi_s^3}{3} - V_{go}(\psi_d^3 - \psi_s^3)\right) \quad (10)$$

part of the gate current is given as [11]

$$J_{PF} = C \cdot E \cdot exp(\alpha + \beta\sqrt{E}) \quad (11)$$

where $\alpha = -\phi_d/V_t$, ϕ_d being the barrier height for electron emission from the trap state, and $\beta = \sqrt{q/\pi\epsilon_s}/V_t$. ϵ_s is the semiconductor permittivity, C is a parameter dependent on the trap concentration and E is the electric field given as $\frac{q\sigma_p - C_g(V_{go} - \psi)}{\epsilon_s}$; σ_p being the effective polarization charge. Using (5) we can get the current due to the Poole-frenkel component as $I_{PF} = W\int_0^L J_{PF}dx$, which after integration yields (6) where $A = \epsilon_s K(C_g V_t + q\sigma_p)$, $K = 1/(V_{go} - \psi_m + V_t)\psi_{ds})$, $B = \epsilon_s^2 K$ and $J_0 = (2WLCA)e^{\alpha+\beta\sqrt{E}}/(\beta^4 C_g^2)$.

The currents due to the thermionic emission (I_{TE}) and trap assisted tunneling (I_{TA}) can be calculated as (7) and (8) respectively[11] where $J_{TE0} = A^* T^2 exp\left(-\frac{\phi_b}{V_t}\right)$, J_{TA0} is the reverse saturation current density, $J_1 = WLJ_{TE0}K$ and $J_2 = WLJ_{TA0}K$. A^* is the effective Richardsons constant, ϕ_b is the Schottky barrier height, η is the ideality factor and V_0 is a fitting parameter.

D. Noise models

ASM-HEMT also includes analytical models for low frequency flicker noise [12] and high frequency thermal noise [13]. These noise models are based on the surface potential core as described in subsection A. The flicker noise model is based on an unified approach taking both the carrier number fluctuation and the mobility fluctuation into account. The drain current noise power spectral density (PSD) for the flicker noise, S_{if}, is given as (9); where $P_1(f) = kT/(WL^2 f^{EF}$, f is the frequency of operation, EF, Γ_1, Γ_2 and Γ_3 are parameters; and $n_{s/d}$ represent the source/drain charge densities. The thermal noise model is based on the approach by Klaassen and Prins, which gives the drain current noise PSD, S_{it}, as (10).

E. Temperature dependance

ASM-HEMT includes temperature dependencies for mobility, velocity saturation, cut-off voltage, subthreshold slope, drain induced barrier lowering, and source and drain access region resistances; along with a self-heating model. The noise models are also temperature dependent.

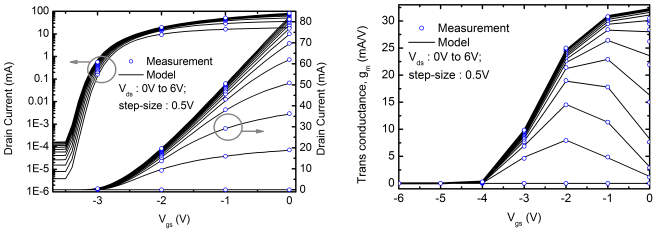

Fig. 1: Figures show the DC characteristics: (a) Drain current in the log scale (left y-axis) and linear scale (right y-axis) versus gate voltage for different drain biases; (b) Transconductance for the same bias range. The measurement is for a GaN HEMT with

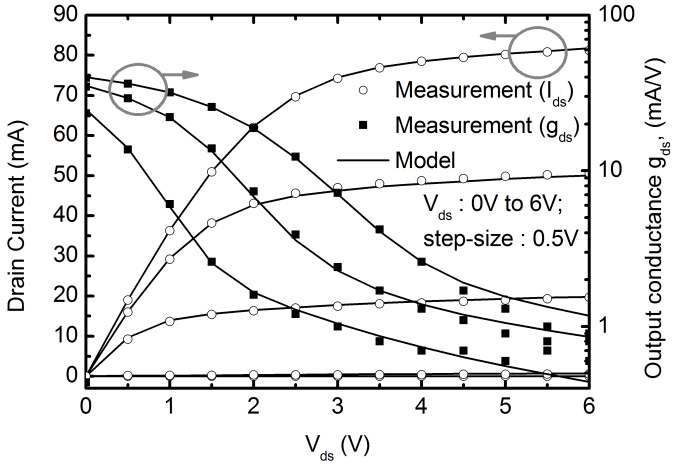

Fig. 2: Drain current (left y-axis) and g_{ds} (right y-axis) with drain to source voltage for different gate biases. The measurement is for a GaN HEMT with $L_G = 1\mu m$, $W = 2 \times 100\mu m$, grown on a $350\mu m$ thick sapphire substrate.

III. Results and Discussion

Fig. 1 shows the measured data for a GaN HEMT ,with gate length $L_G = 1\mu m$ and width $W = 2 \times 100\mu m$ grown on a $350\mu m$ thick sapphire substrate, along with the simulated result obtained from our model for the drain current 1a and the transconductance 1b, with increasing gate bias. Fig. 2 presents

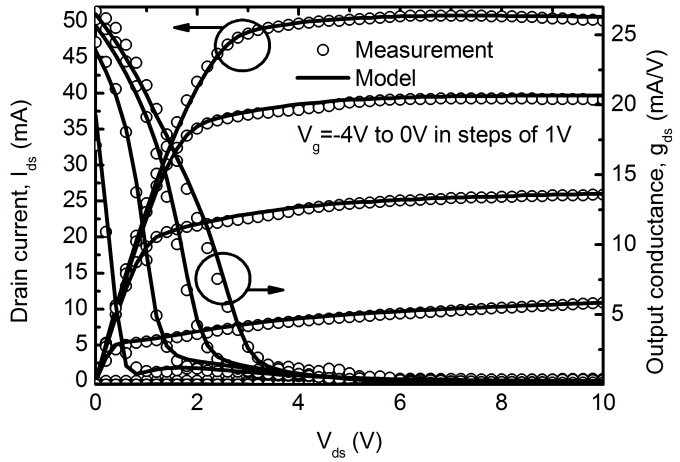

Fig. 3: Drain current (left y-axis) and output conductance (right y-axis) as a function of drain voltage for different gate voltages. The measured data is for a GaN HEMT with $L_G = 200nm$, $W = 50\mu m$, $L_{SG} = 600nm$ and $L_{DG} = 700nm$.

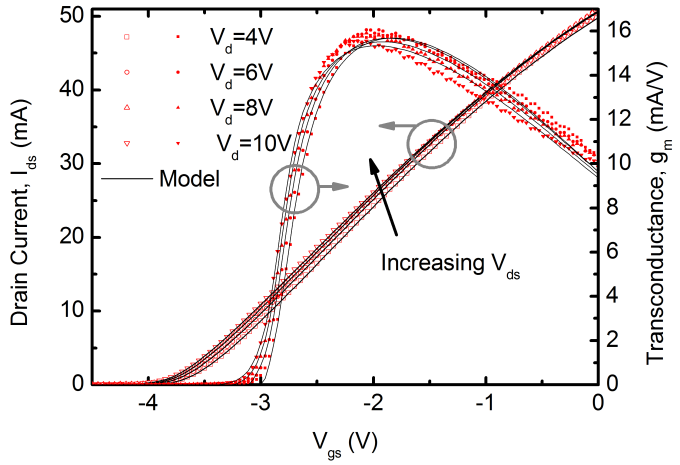

Fig. 4: Drain current (left y-axis) and transconductance (right y-axis) as a function of gate voltage for different drain voltages. Measurement is for a GaN HEMT with $L_G = 200\mu m$, $W = 50\mu m$, $L_{SG} = 600nm$ and $L_{DG} = 700nm$.

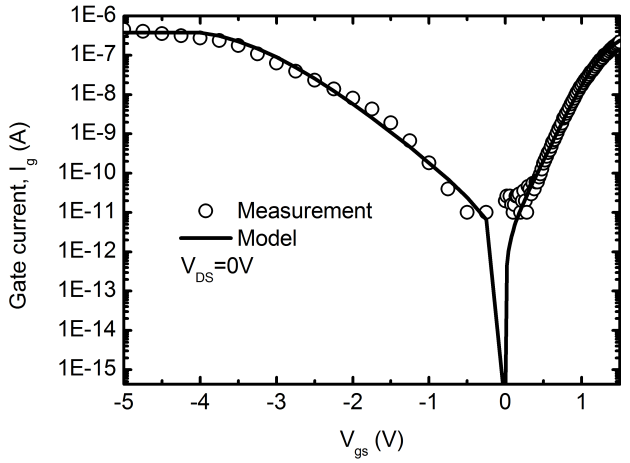

Fig. 5: Gate current for $I_{ds} = 0A$ for a wide gate voltage range. The negative gate voltage region shows the Poole-Frenkel component whereas the positive gate voltage region illustrates the thermionic emission component of the gate current. Measurements are done on a GaN HEMT with $L_G = 200\mu m$, $W = 50\mu m$, $L_{SG} = 600nm$ and $L_{DG} = 700nm$. The model gives zero current at zero bias i.e. $V_{GS} = V_{DS} = 0V$; $I_{DS} = 0A$

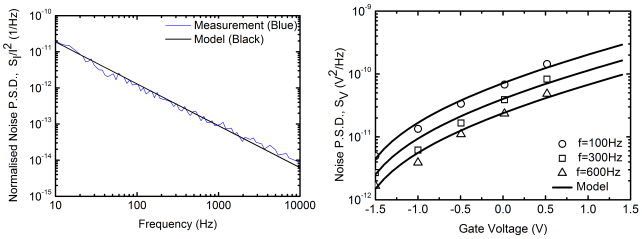

(a) (b)

Fig. 6: Flicker noise modeling: (a) Normalised noise spectral density (1/Hz) versus frequency [12] at $V_{gs}VOFF = 1V$ and $V_d = 1V$ for a $0.7\mu m$ GaN device; (b) Noise spectral density versus gate bias [12] at $f = 0.1KHz, 0.3KHz and 0.6KHz$ and $Vd = 0.5V$ for a $1\mu m \times 50\mu m$ GaN device.

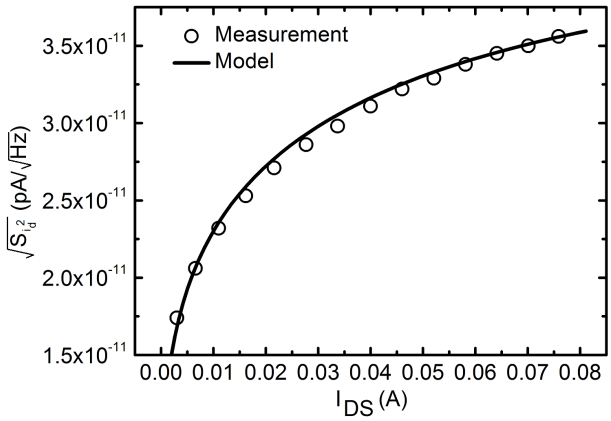

Fig. 7: Thermal noise modeling: Drain current noise PSD with varying drain current [13] for $V_{ds} = 9V$ and $f = 9GHz$. Measured data is for a $2 \times 100\mu m$ device [14].

the measured data and model results for the drain current (left y-axis) and the output conductance (right y-axis) with increasing drain voltage for the same device.

The gate current model is validated with measured data from a GaN HEMT with $L_G = 200nm$, $W = 50\mu m$, $L_{SG} = 600nm$ and $L_{DG} = 700nm$. For this device, Fig. 3 shows the drain current and the output conductance with varying drain voltage and Fig. 4 shows the drain current and transconductance for varying gate voltage. The parameters extracted from these DC curves is then used to simulate the gate current. Fig. 5 shows the gate current with varying gate voltage for the complete operable bias ranges, highlighting the Poole-Frenkel (negative V_{gs}) and the thermionic emission (positive V_{gs}) components respectively.

The validation of the flicker and thermal noise models are shown in Fig. 6 and Fig. 7. Fig. 6a shows the drain current noise PSD for low frequency, highlighting the frequency dependence of the flicker noise model along with measured data for a $0.7\mu m$ GaN device; whereas Fig. 6b shows the bias dependence of the same noise model for a $1\mu m \times 50\mu m$ GaN HEMT. Fig. 7 shows the bias dependence of the drain current noise PSD for the high frequency thermal noise model. The measured data presented in this figure is for a $2 \times 100\mu m$ GaN device [14].

Fig. 8 shows the drain current (left y-axis) and the transconductance (right y-axis) for a $250nm$ GaN HEMT [15] at different temperatures. The model is able to predict the temperature

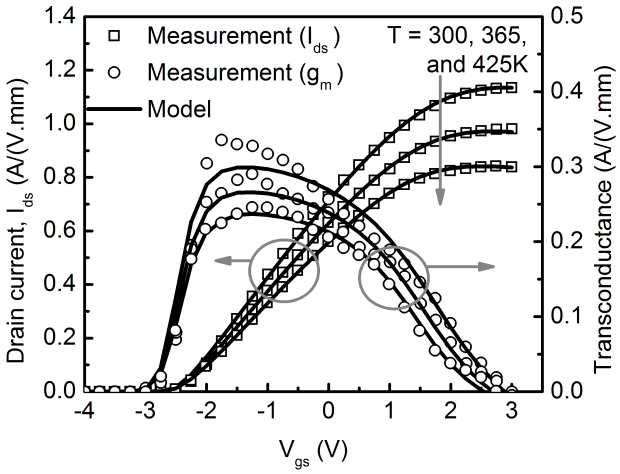

Fig. 8: Plot of the drain current (left y-axis) and the transconductance (right y-axis) with gate voltage for $V_{ds} = 7V$ at three different temperatures. The measured data is for a AlGaN/GaN device with $L_G = 250nm$ [15].

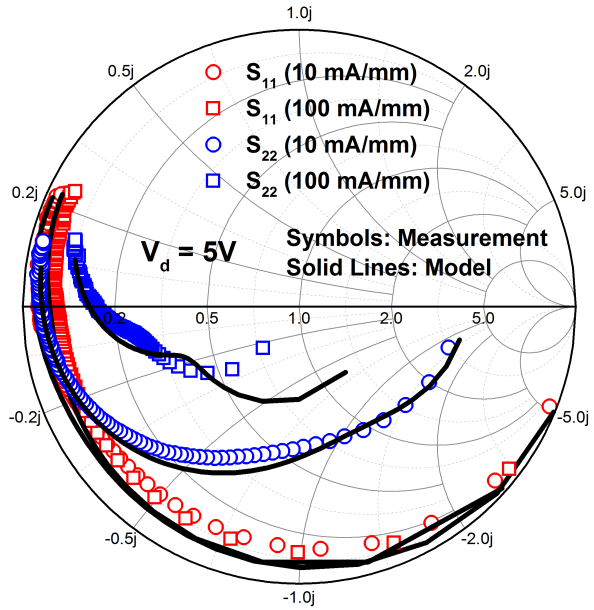

Fig. 9: Plot of the S-parameters for $I_{ds} = 10mA/mm$ and $I_{ds} = 100mA/mm$ with $V_{ds} = 5V$. The measured data is for a GaN RF device with 10 fingers and $90\mu m$ width.

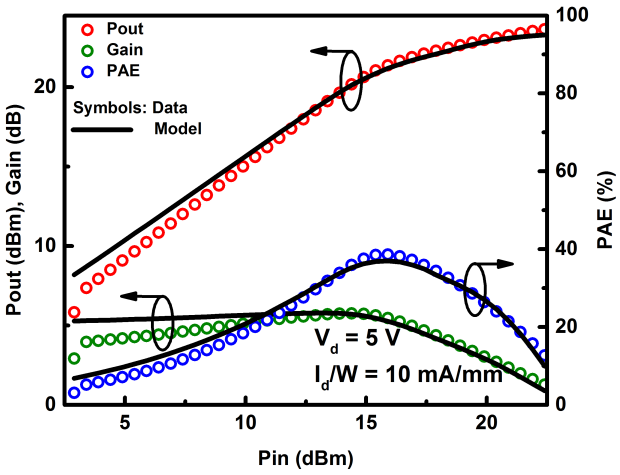

Fig. 10: Plot of the power output, gain and power added efficiency for $I_{ds} = 10mA/mm$ and $I_{ds} = 100mA/mm$ with $V_{ds} = 5V$. The measured data is for a GaN RF device with 10 fingers and $90\mu m$ width.

dependance well and matches well with the measurement. Fig. 9 shows the S-parameter measurements along with the model results for a GaN RF device with 10 fingers and $90\mu m$ width. The measured data is for two bias conditions of $I_{ds} = 10mA/mm$ and $I_{ds} = 100mA/mm$ with $V_{ds} = 5V$. Fig. 10 shows the power seep measurements along with the model predictions from harmonic balance simulations for the same device and bias conditions as Fig. 9. As can be seen, the model accurately captures the gain compression phenomenon which is important for the operation range of such devices.

IV. Conclusion

We have presented an accurate and analytical surface potential based GaN HEMT model. The model has been validated with data for GaN devices of different geometries and shows good match with the measurement. The model is currently being considered for industry standardization by CMC.

Acknowledgment

This work was partially funded by Ramanujan fellowship research grant; DST fast-track scheme for young scientists; Indian Space Research Organisation; and the Council of scientific and Industrial Research (CSIR), India.

References

[1] I. Angelov et. al., *IEEE MTT*, Dec. 1992.
[2] T. Sadi et. al., *IEEE ESSDERC*, 2010.
[3] Y. Long et. al., *IEEE Trans. MTT*, Oct. 2012.
[4] A. Koumdymov et. al., *IEEE TED*, Mar. 2008.
[5] M. Li et. al., *IEEE TED*, Jan. 2008.
[6] X. Cheng et. al., *IEEE TED*, Dec. 2009.
[7] S. Khandelwal et. al., *IEEE TED*, Oct. 2012.
[8] S. Khandelwal, *Ph.D. dissertation*, Dept. Electron. Telecom., NTNU, 2013.
[9] S. Khandelwal et. al., *IEEE TED*, Oct. 2013.
[10] S. Oh et. al., *IEEE Journ. Solid-State Circuits*, Aug. 1980.
[11] S. Ghosh et. al., *IEEE TED*, Feb. 2015.
[12] A. Dasgupta et. al., *IEEE JEDS*, Jun. 2014.
[13] A. Dasgupta et. al., *IEEE MWCL*, accepted Mar. 2015.
[14] M. Thorsell et.al., *IEEE MTT*, Jan. 2009.
[15] S. Vitanov et. al., *Solid-State Electronics*, Oct. 2010